

Long-Term Active Corrosion Protection of Damaged Coated-AA2024-T3 by Embedded Electrospun Inhibiting Nanonetworks

Christian D. Dieleman, Paul J. Denissen, and Santiago J. Garcia*

In this work, a new concept is introduced for active corrosion protection at damaged sites aiming at overcoming existing limitations of currently proposed strategies based on dispersed inhibitor-loaded nanocontainers in coatings. The underlying principle is based on the formation of low-density and/or humidity responsive interconnected paths of inhibitor in the coating, what is called *inhibiting nanonetworks*. Such an approach allows for (on-demand) long-term local supply of corrosion inhibitor at the damage site. For the proof-of-concept, water responsive inhibiting nanonetworks based on polyvinyl alcohol and two known efficient corrosion inhibitors for AA2024-T3 (cerium chloride and lithium carbonate) using electrospinning are developed. The *inhibiting nanonetworks* are obtained by subsequently embedding the electrospun fiber mats in thermoset epoxy coatings applied on AA2024-T3. The coated panels are scratched and exposed to NaCl solutions for a month while continuously monitoring the protective properties electrochemically and optically in a hyphenated setup. The effect of the corrosion inhibitor type and the partial crosslinking of the mat on release and protection are analyzed. Protection levels at relatively big damaged sites are obtained for at least a month immersion thereby proving the benefits of high inhibitor quantities continuously released in time.


1. Introduction

The most common method to protect metallic structures against their natural tendency to undergo reduction-oxidation reactions relies on coatings loaded with corrosion inhibitors or sacrificial particles. The search for strategies alternative to traditional ones using highly efficient but toxic inhibitors such as hexavalent chromates led to the development in the last two decades of multiple concepts using nanoparticles loaded with inhibitors. These carriers serve two main purposes: (i) isolate

the inhibitor from the matrix so unwanted reactions do not take place; and (ii) allow for the controlled release of the inhibitor (controlled kinetics or on-demand release). Many materials, shapes, sizes, and triggers have been developed using this basic principle ranging from microcapsules and nanocapsules relying on delamination to initiate the redox triggered release, to loaded nanosized porous zeolites and halloysite nanotubes where release relies on leaching and ion exchange.^[1] Despite the clear success of the concept, two intrinsic limitations can be identified: (i) loading in nanoparticles is limited and bound to carrier-inhibitor pairs; and (ii) inhibitor release at a damage site greatly depends on particle size, release trigger, loading, and distribution.^[2] As a consequence the long-term protection and protection at relatively big damages is compromised.^[2b] Here we propose an alternative strategy based on the formation of low-density and/or humidity responsive interconnected paths of inhibitor inside

the coating (i.e., *inhibiting nanonetworks*) as a way to overcome the above limitations. Such a strategy is based on recent findings by Hughes et al.^[3] who recently attributed high inhibition of Cr(VI)-based coatings to the formation of inhibitor interconnected clusters and low density regions in the coating, thereby confirming previous modelling works.^[2] In order to experimentally proof the validity of the concept we used the well-established process of electrospinning as the method to manufacture the responsive nanofiber mats containing corrosion inhibitors to form the inhibiting nanonetworks in the coatings. During the relatively simple process of electrospinning a membrane or fiber mat of polymeric fibers can be produced by applying an electric field between a spinneret, usually a needle of a syringe filled with polymer solution, and a grounded conductive collector.^[4] By controlling the process parameters, spinning setup complexity, and the polymer solution physical properties, a large amount of geometries can be designed making it a suitable process for the design of membranes, drug delivery systems, and carriers of liquid self-healing agents for composites among others.^[5] Cu-rich aluminum alloy AA2024-T3 is here used as the substrate to prove the corrosion inhibiting potential of the concept. This highly used aerospace grade aluminum alloy is known for its high corrosion

C. D. Dieleman, P. J. Denissen, Dr. S. J. Garcia
 Faculty of Aerospace Engineering
 Delft University of Technology
 Kluyverweg 1, 2629 HS, Delft, The Netherlands
 E-mail: s.j.garciaespallargas@tudelft.nl

 The ORCID identification number(s) for the author(s) of this article can be found under <https://doi.org/10.1002/admi.201800176>.

© 2018 The Authors. Published by WILEY-VCH Verlag GmbH & Co. KGaA, Weinheim. This is an open access article under the terms of the Creative Commons Attribution License, which permits use, distribution and reproduction in any medium, provided the original work is properly cited.

DOI: 10.1002/admi.201800176

susceptibility induced by the strong local microgalvanic couples at intermetallic (IM)-matrix interfaces leading to extensive literature related to its corrosion and corrosion inhibition mechanisms.^[5] Among the different corrosion inhibitors proposed to replace hexavalent chromium, Ce³⁺ based inhibitors such as Cerium chloride (CeCl₃) have attracted significant well-deserved attention due to their cathodic inhibiting character.^[6a] Nevertheless, their high reactivity with epoxy-amine binders highly hampers the cerium release and limits their ultimate application in protective coatings, thereby being a very good inhibitor model for the proof-of-concept here presented. In order to explore the applicability of the (electrospun) inhibiting nanofiber concept to other inhibitors lithium carbonate (Li₂CO₃) was used due to the recently demonstrated high potential of Li-salts as highly efficient chromate replacements.^[7] The nanofiber mats were produced from water soluble poly(vinyl alcohol) (PVA) as this allows relatively easy spinning but also easy control of the release kinetics by partial crosslinking leading to embedded humidity responsive regions of low density for faster inhibitor leaching. In this work we present the potential of the concept of *inhibiting nanonetworks*, here produced by electrospinning, as a new efficient concept to protect highly corrosion-susceptible alloys for long immersion times in corrosive media.

2. Results and Discussion

2.1. Manufacturing of *Inhibiting Nanonetworks* by Electrospinning (Inhibitor Loading)

The details on the electrospinning setup and the used process can be found in the Experimental Section and Section S1 (Supporting Information). The scanning electron microscope (SEM) images in **Figure 1a–c** confirm that the correct choice and control of parameters allows electrospinning nanofiber mats free of visible defects such as holes, agglomerates or solvent droplets. The spinning process had to be adapted when different inhibitors and concentrations were used in order to avoid spinning instabilities and obtain comparable fiber mats as shown in the Experimental Section and the Section S1 (Supporting Information). The uniform fiber mats showed small diameter differences as function of the inhibitor content ranging generally from 300–400 nm in the PVA fiber to 400–600 nm when the inhibitors were used. The thickness differences as well the presence of nods and less fiber uniformity in the case of inhibitor-containing solutions can be attributed to the increase in solution conductivity when the inhibiting salts are used and when the spinning process is not fully optimized.^[4,8]

The presence of cerium chloride inhibitor in the nanofiber mats was confirmed by SEM-energy dispersive X-ray spectroscopy (EDS) as shown in **Figure 1d** by the clear appearance of chlorine peaks at 2.5 and 2.9 keV and characteristic cerium peaks in the region between 4.5 and 6.5 keV. Such peaks become more prominent when the inhibitor loading increased from 5 to 10 wt% w.r.t. PVA (**Figure 1d**). The absence of particle agglomerates and highly localized cerium signals in the elemental maps (**Figure S2a**, Supporting Information) confirm the good distribution of the inhibitor. Unfortunately, the Li inhibitor could not be traced back with EDS due to its low

energy of characteristic radiation. Nevertheless, the results with Ce, the fiber homogeneity and the electrochemical tests shown in the subsequent sections are strong indications suggesting that the Li-inhibitor was also incorporated to the electrospun fiber matrix.

2.2. Release Kinetics from the Free Standing Electrospun Nanonetworks (Inhibitor Release)

The release kinetics of cerium ions was monitored by UV–vis spectroscopy. Unfortunately, it was not possible to monitor Li₂CO₃ release by the same technique and was therefore not part of this study. As shown by Soestbergen et al. cerium has a distinct absorbance spectrum in UV–vis with several excitation peaks of which the most prominent and sensitive one is located at $\lambda = 252/253$ nm. The intensity of this absorption peak shows a linear relationship with the concentration of cerium ions for concentrations up to at least 0.6×10^{-3} M in solution thus allowing for the quantification of cerium release from a carrier in solution after a calibration curve is set.^[9] Similarly, PVA also dissolves in water leading to light absorption in the wavelength range $\lambda < 240$ nm. In the case of the PVA-cerium loaded fibers the UV peaks related to cerium are influenced by the PVA signal thereby leading to an overestimation in the quantification of the cerium release. In order to solve this limitation, a subtraction procedure was implemented as explained in the Supporting Information (Section S3, Figures S3 and S4) leading to a more accurate quantification of the cerium release kinetics.

2.2.1. Effect of the Inhibitor Loading on the Release Kinetics

Figure 2 shows the cerium release profiles of fiber mats containing 5 and 10 wt% cerium chloride w.r.t. PVA normalized to 1 mg of fiber sample weight (**Figure 2a**) and to the theoretical maximum release (**Figure 2b**). As expected, the fibers loaded with 10 wt% cerium lead to two times more cerium released than those with 5 wt%. Moreover, in agreement with the Fick's law for steady-state diffusion, the fibers with a higher Ce content lead to a faster initial Ce release (**Figure 2a**). Interestingly, although the release of cerium occurs within 30 min of immersion, the PVA fiber full dissolution does not occur until 2 h immersion as a small amount of gelled polymer residue was visually observed after the immersion test. Nevertheless, during the release experiments, about 10 wt% of the theoretical cerium content was not released (**Figure 2b**). This suggests some chemical interactions between PVA and Ce³⁺ or measurements errors in the preparation of the cerium-PVA water solutions due to the high hygroscopic nature of the CeCl₃. The high reproducibility of the results points nevertheless at the former as the main cause for the incomplete theoretical release although future work will be necessary to clarify this point.

2.2.2. Effect of PVA-Crosslinking on the Release Kinetics

In order to control the inhibitor release kinetics using the same fiber matrix a crosslinking posttreatment of the PVA fiber mats

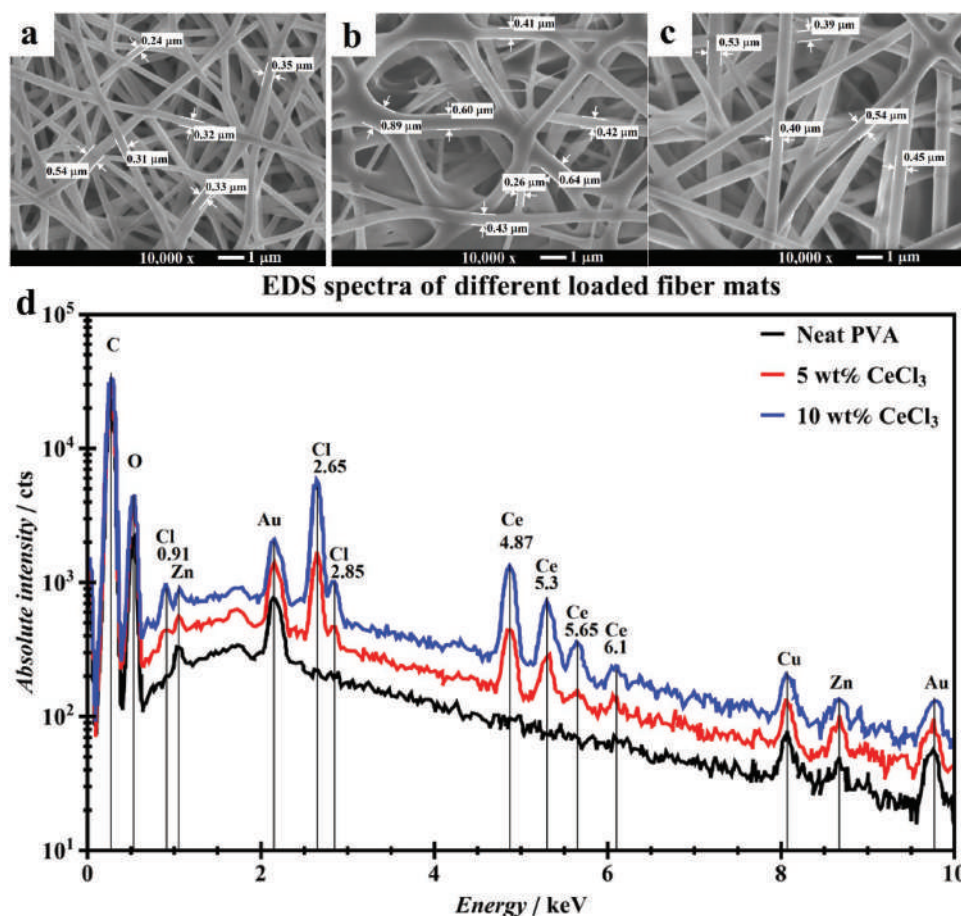


Figure 1. SEM images of a) PVA electrospun nanofiber, b) PVA fibers loaded with 10 wt% CeCl₃, and c) PVA fibers loaded with 10 wt% Li₂CO₃. All fibers were produced from an 8 wt% PVA water solution. Scale bar is 1 μm, magnification 10 000 ×. Panel (d) shows the EDS spectra of the PVA networks loaded with increasing concentration of CeCl₃. Clear Ce (4.87, 5.3, 5.65, 6.1 keV) and Cl (0.91, 2.65, 2.85 keV) peaks can be observed and increase with the inhibitor loading.

using glutaraldehyde (GA) was employed as explained in the Experimental Section and Figure S5 in Section S4 (Supporting Information). During this crosslinking reaction the hydroxyl groups react with the aldehyde groups to form acetal bridges between the PVA chains thereby (partially) crosslinking the PVA.^[10] To obtain different crosslinking degrees two acetone solutions containing were prepared and the crosslinking effect was assessed by Fourier transform infrared spectroscopy (FTIR) and SEM before and after exposure to water. Changes in the FTIR spectra (Figure S6, Supporting Information) confirmed that crosslinking reactions took place as reported in literature and discussed in the Section S4 (Supporting Information).^[11] No significant differences in the FTIR peak identification were found when the PVA fiber mats contained cerium thereby suggesting a minor influence of these ions in the crosslinking process. SEM confirmed that the crosslinking posttreatment did not affect the fiber thickness when the crosslinking bath contained high GA concentrations (Figure 3a,b). On the contrary, low GA concentration in the crosslinking bath led to shape loss of the fibers (swelling) due to an insufficient or slow crosslinking process followed by swelling and local dissolution in presence of acetone in the crosslinking bath (Figure 3c). EDS analysis showed similar intensity levels of Ce peaks in the fibers

after the crosslinking process indicating that at least most of the Ce remained in the fibers during crosslinking (Figure S2b, Supporting Information). This last point was further supported by the higher Ce release observed in the UV–vis for the low crosslinked mats (Figure 2c,d). The effect of the crosslinking was further assessed by adding a water droplet on top of the different fiber mats for one hour. In this test the noncrosslinked PVA fiber quickly dissolved and the partially crosslinked fiber mat (10×10^{-3} M GA) significantly swell leading to a cohesive PVA film (Figure 3d). On the other hand, the fiber mats crosslinked with 30×10^{-3} M GA showed a fiber diameter and shape similar to those prior to water exposure with some swelling (Figure 3e) thereby confirming previous reports.^[10] and presumably allowing for a partial release of the inhibitor, as shown later on.

The effect of the crosslinking step on the release kinetics was further investigated by UV–vis and shown in Figure 2c,d. In these figures it can be clearly seen that the final concentration and release fraction decreased with the crosslinking increase combined with a change in release kinetics. When compared to the noncrosslinked system it was found that about 10% less inhibitor was released when partially crosslinked (10×10^{-3} M GA) while 40% less inhibitor

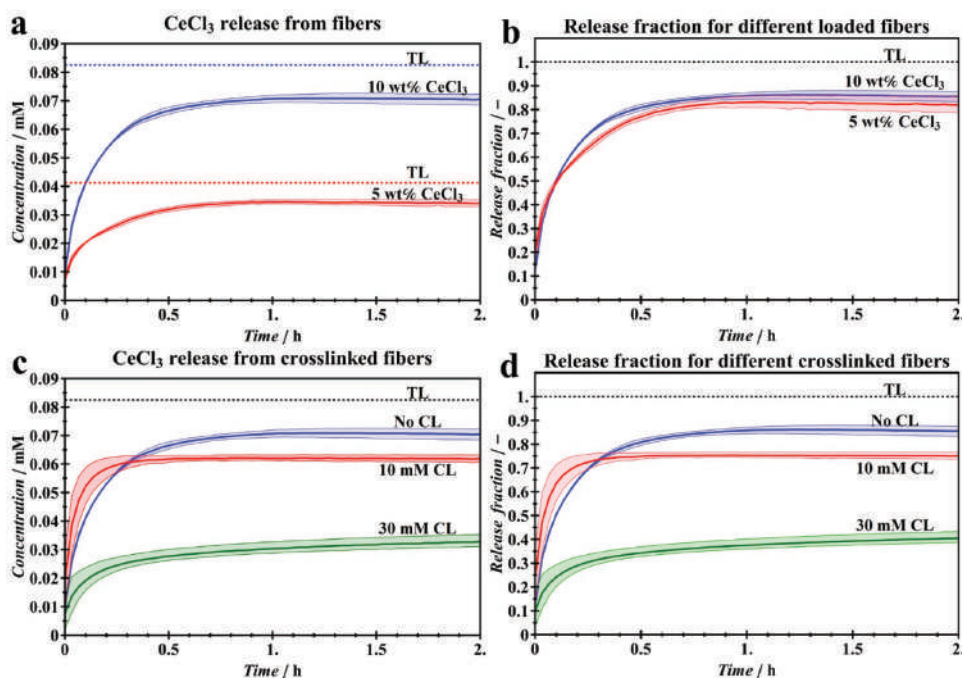


Figure 2. Release kinetics of CeCl_3 from PVA nanonetworks as affected by a,b) inhibitor loading and c,d) amount of PVA crosslinking. The diffuse colored areas around the main lines indicate the measurement deviation for a number of three measurements. TL dotted line marks the theoretical maximum release. Differences in inhibitor loadings affect final concentration but not the mechanism of release. Crosslinking affects both the final concentration as well as the release mechanism. The release of cerium ions was followed at wavelength $\lambda = 253 \text{ nm}$. A correction on the measured absorbance was applied as exposed in the Section S3 (Supporting Information).

was released in the case of the highly crosslinked network ($30 \times 10^{-3} \text{ M GA}$) after 2 h immersion. These results further confirm the crosslinking of the fiber mats leading to certain entrapment of cerium ions in the PVA-GA network and no significant release of Ce into the crosslinking bath during this process. A detailed fitting and analysis of the release curves with an extended Peppas-Korsmeyer release model accounting for the influence of swelling and dissolution on the first stages of release and concentration control release is shown in the Supporting Information (Section S5, Figure S7).^[12] The fitting parameters confirm the deviation from Fickian diffusion in the case of noncrosslinked mats due to swelling and dissolution and a closer to Fickian behavior in the case of the most crosslinked fibers. These preliminary results confirm the possibility to modify and control the inhibitor release kinetics from the electrospun mats and therefore from the inhibiting nanonetworks in the coating.

2.3. Corrosion Protection at Damaged Sites of Coated AA2024-T3 by Inhibiting Nanonetworks

Table 1 shows the characteristics of the different coatings prepared as indicated in the Experimental Section and used in this work to evaluate (i) the fiber mat crosslinking effect and (ii) the effect of the inhibitor type contained in the fiber mat (CeCl_3 or Li_2CO_3). All coatings had a multilayer assembly (see the Experimental Section) consisting of (i) a base layer to prevent fast delaminations, (ii) an electrospun inhibiting nanonetwork,

and (iii) a protective topcoat as represented in Figure 3f. For the corrosion evaluation we used a hyphenated optical and electrochemical setup allowing us to simultaneously monitor electrochemical responses such as open circuit potential (OCP) and electrochemical impedance by electrochemical impedance spectroscopy (EIS) and time-lapsed optical images of the exposed area under immersion as reported elsewhere.^[13] This hyphenated approach allowed for a more detailed analysis of the ongoing degradation processes and the protection levels achieved. The EIS results of the intact coatings can be found in Figure S8 (Supporting Information) and show good barrier protection for all coatings.

Figure 4 shows the Bode plots of impedance and phase angle at different immersion times of different samples shown in Table 1. The unloaded sample (PVA) and the sample containing a cerium-loaded but uncrosslinked fiber mat (10Ce) are shown up to 10 d immersion due to the loss of overall protection within this period. The epoxy coating without fibers behaved similar to the PVA coating system and can be seen in Figure S9 of the Supporting Information. On the other hand, the samples containing cerium-loaded crosslinked fibers (10CeCL) and lithium-loaded uncrosslinked ones (10Li) are shown up to 4 weeks of immersion due to their overall good corrosion protection behavior. **Figure 5a,c** shows the OCP evolution with the immersion time which is directly related to the surface composition and delaminations taking place: OCP values close to those of bare AA2024-T3 ($-0.55 \text{ V vs Ag/AgCl}$) suggest protection and OCP values dropping to $-0.7/-0.9 \text{ V}$ versus Ag/AgCl suggest dealloying and delamination.^[14-16]

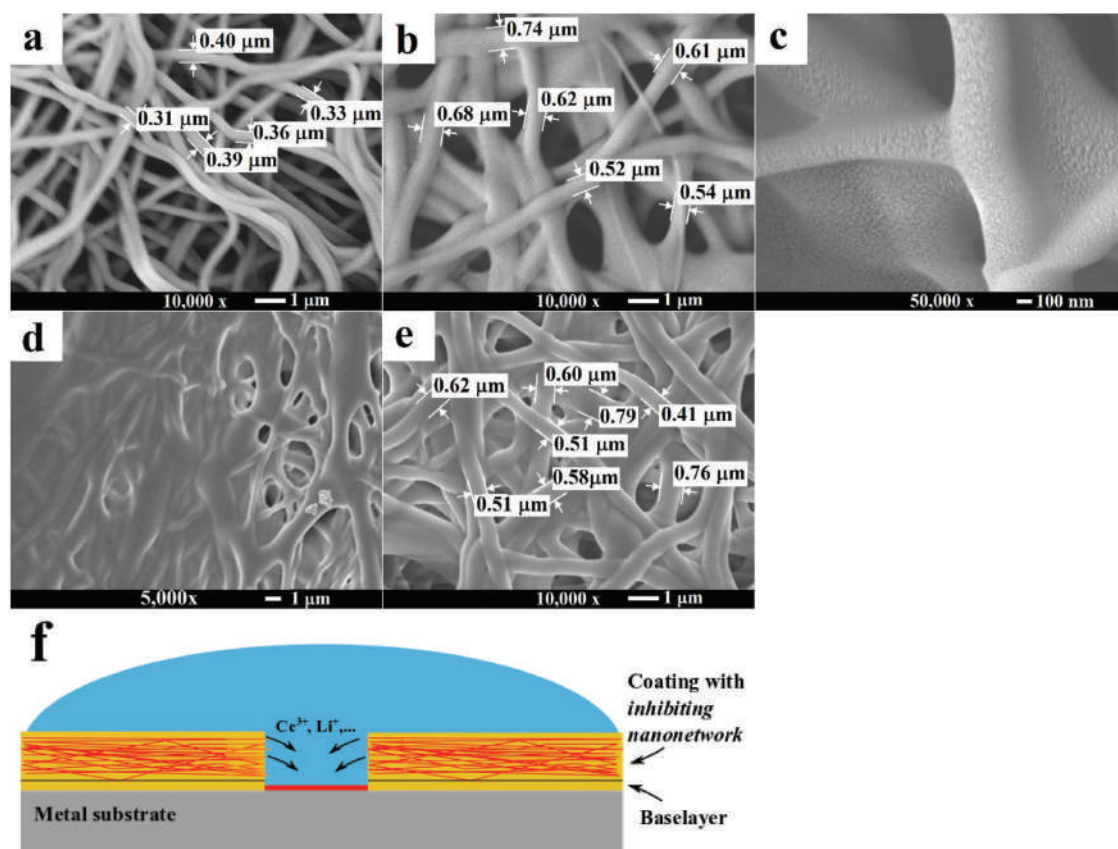


Figure 3. SEM microscopy images of PVA fiber mats crosslinked for 24 h: a) unloaded fiber in 30×10^{-3} M GA, b) cerium-loaded fiber mat crosslinked with 30×10^{-3} M GA, and c) cerium-loaded fiber mat crosslinked with 10×10^{-3} M GA. Microscopy images (d) and (e) show the cerium loaded fiber mats crosslinked with 10 and 30×10^{-3} M GA, respectively, after 1 h exposure to water. Partially crosslinked fibers show major swelling and partial dissolution, while for a higher degree of crosslinking, the fiber shape is maintained after exposure to water. Panel (f) shows an idealized scheme of the embedment of the fiber mats in epoxy coatings leading to the inhibiting nanonetworks and their protective mechanism.

Figure 5b,d shows the low-frequency total impedance ($|Z|$ at 0.01 Hz) time evolution, which is typically related to the activity at the metallic substrate at damaged site and therefore to the extent of protection.^[17a] **Figure 6** shows the microscopy images of the scratched samples at different immersion times of 0, 2, 24 h, 1 week and, if available, 4 weeks. In this figure several features of relevance can be observed such as the initial scratch, the water ingress in the fiber mats (as a change in color due to the refraction index alterations), delaminations and corrosion activity at the scribe (dark areas). In the following sections these figures will be discussed to investigate the effect of inhibitor type and the crosslinking of nanonetworks on the corrosion protection at damaged sites.

Table 1. Different coating samples that were electrochemically characterized with their most important coating characteristics.

Sample name	Base layer [μm]	Fiber mat [μm]	Crosslinked fibers	Total thickness [μm]	Inhibitor type
PVA	7 ± 1	60 ± 5	–	180 ± 15	–
10Ce	7 ± 1	50 ± 5	–	105 ± 15	CeCl ₃
10CeCL	6 ± 1.5	60 ± 5	10 × 10 ⁻³ M GA	180 ± 20	CeCl ₃
10Li	6 ± 1.5	60 ± 5	–	140 ± 15	Li ₂ CO ₃

2.3.1. Effect of Inhibitor Type Using Noncrosslinked Inhibiting Networks

Figure 4a–c allows comparing the inhibiting behavior of Cerium and Lithium inhibitors when embedded in an epoxy coating by means of the fiber mats. As expected, the unloaded sample shows very poor protective properties as seen by a continuous decrease in impedance at frequencies between 10² and 10⁻² Hz and a relatively narrow phase angle distribution with continuous shifts downward thereby showing the nihil or negligible inhibiting effect of the dissolved PVA. In contrast, both 10Ce and 10Li samples show a broader phase angle distribution with no low-frequency increase typically related to pitting, and a high impedance at frequencies below 10² Hz for long periods of time, all indicating a good corrosion protection.^[17]

In order to better visualize the key differences between these samples we opted to plot the low-frequency total impedance ($|Z|_{0.01 \text{ Hz}}$) and OCP time-evolution as shown in Figure 5 together with the time-lapse optical images shown in Figure 6. Again, these figures show that the inhibitor-free PVA mat does not lead to any significant protection: (i) OCP is

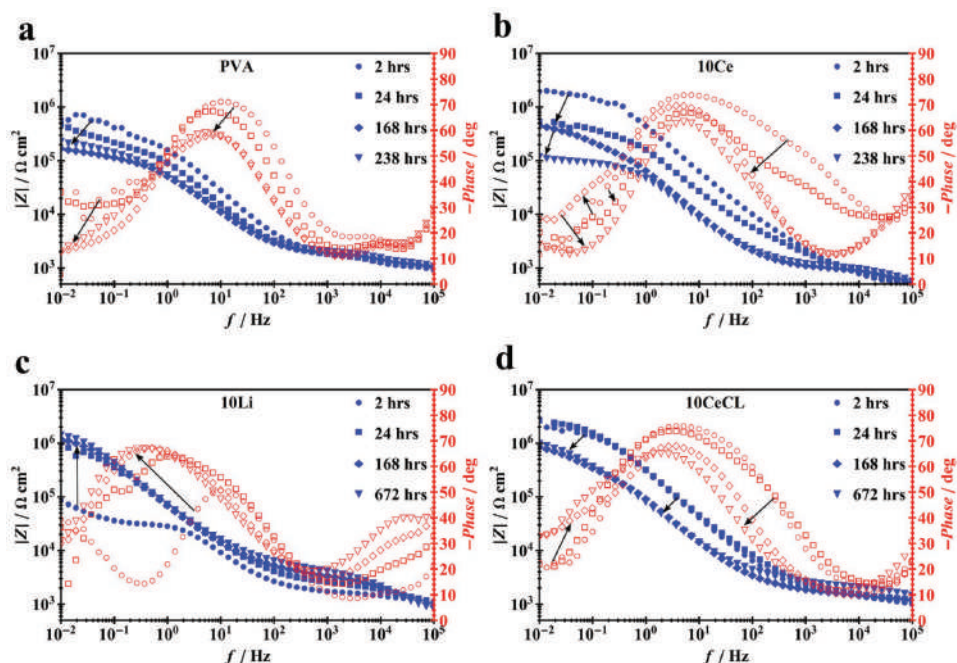


Figure 4. Bode plots showing total impedance ($|Z|$) and phase angle (θ) of four coated samples containing inhibiting nanonetworks from electrospun PVA a) without inhibitor, b) with CeCl_3 uncrosslinked, c) with Li_2CO_3 uncrosslinked, and d) CeCl_3 crosslinked. Arrows indicate trends between the different immersion times indicated in the legend. High impedance values as well as broader and higher phase angles indicate better protection.

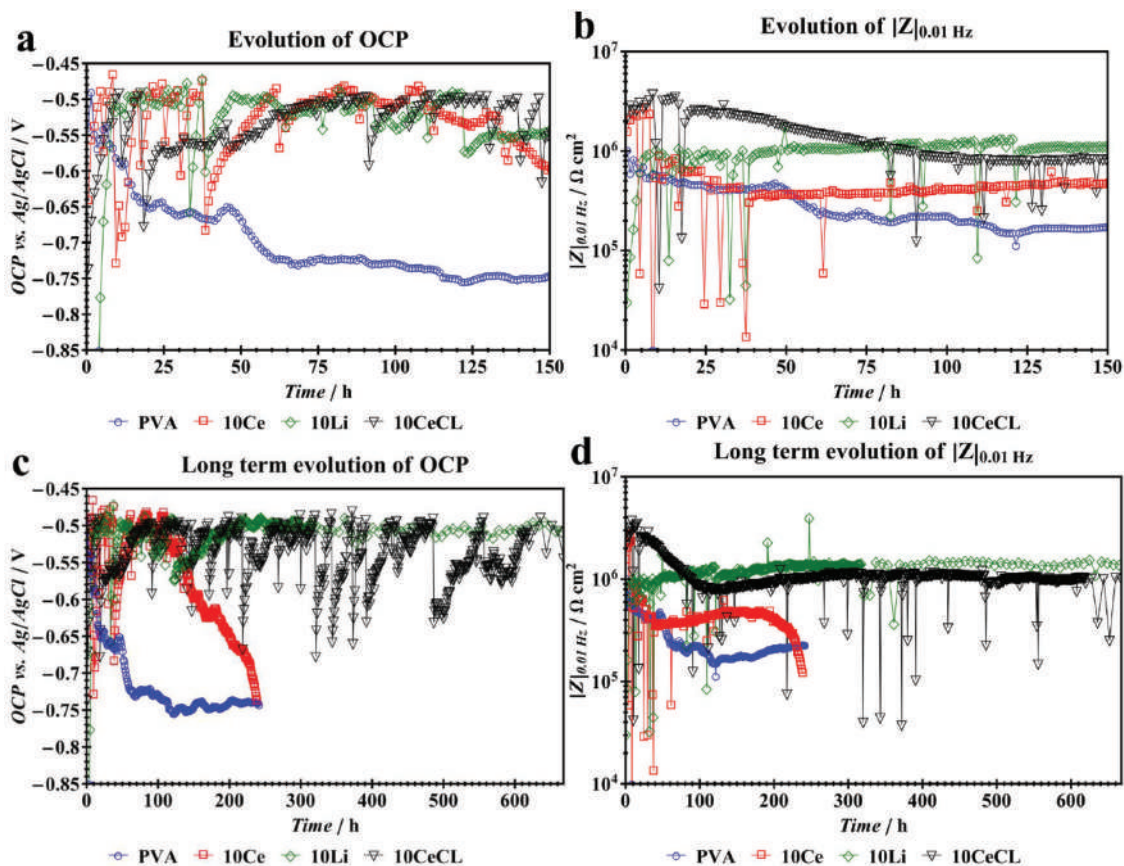


Figure 5. Time evolution of a,c) OCP and b,d) $|Z|_{0.01 \text{ Hz}}$, where (c) and (d) show the whole immersion period.

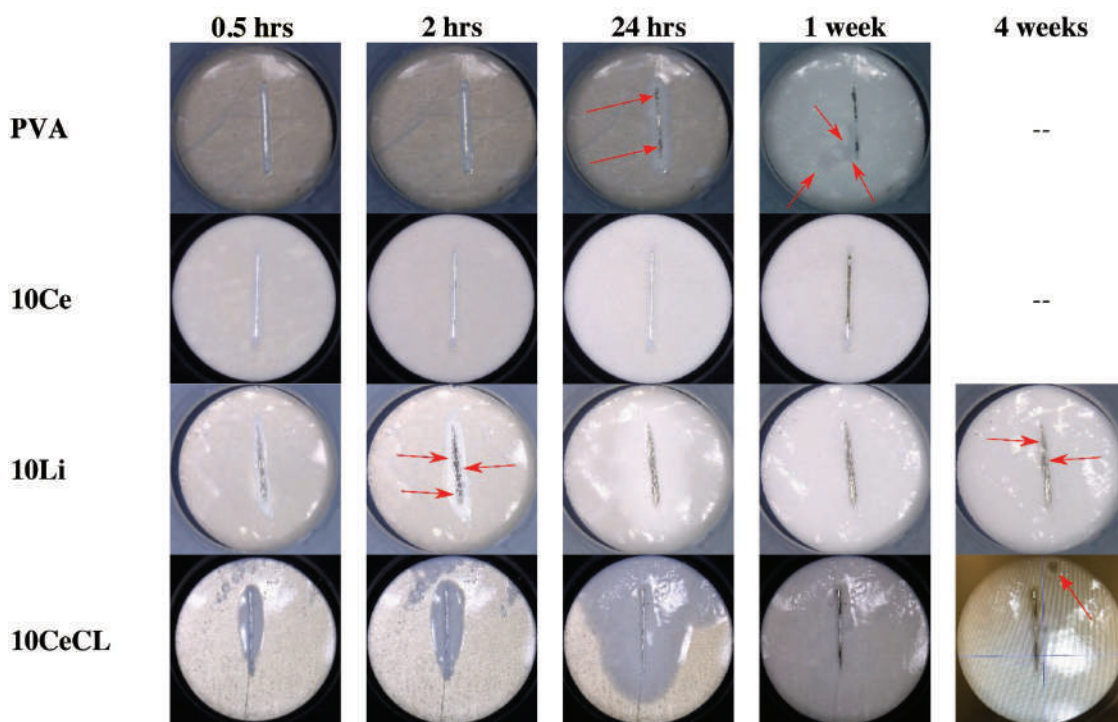


Figure 6. Time-lapse images from the optical feature of the optical-electrochemical setup. Red arrows indicate points of interest such as delaminations and formation of corrosion products. Dark spots at the scribe are related to corrosion attack (oxides and pits). Scratches are 5 mm long and $120 \pm 10 \mu\text{m}$ wide. Note: color changes in the images are due to a combination of the camera setting adapting contrast and brightness and the changes in the coating due to corrosion and water ingress.

continuously dropping toward values of dealloyed aluminum, (ii) the impedance values are almost a full decade lower than those of the inhibitor containing systems, and (iii) the optical images show the formation of corrosion products at the scratch as early as after 24 h and delaminations after 1 week (marked by arrows in Figure 6).

In contrast to the noninhibited sample, the 10Ce sample shows some initial protection by a delay of dealloying observed by OCP (to about 130 h) and initially high impedance values (first 15 h). Protection is nevertheless lost as seen by the subsequent OCP and impedance decrease as well as the appearance of corrosion products in the scratch after 1 week.

A different behavior is observed when lithium inhibitor is used. The 10Li sample shows initially low OCP ($< -0.8 \text{ V}$) and impedance ($\approx 10^4 \Omega \text{ cm}^2$) values suggesting strong dealloying and redox processes at the metal surface. These values nevertheless gradually increase with the immersion time for about 10 h until they reach values that suggest a good substrate protection (-0.5 V , $\approx 10^6 \Omega \text{ cm}^2$) and that remain stable for the whole immersion time (up to 4 weeks). The physical phenomena behind this unusual electrochemical trend is clarified by analyzing the optical images taken during immersion as those shown in Figure 6. The image analysis revealed a strong gas evolution at the scribe just after 2 h immersion and for about 20 h, clear indicator of strong redox processes. After this time, the bubble evolution stops and the scratch remains clean and shiny for several weeks. After 4 weeks immersion light gray deposits, appearing to be of different nature than in the other samples, could be observed. The different results point at the

formation of a stable protective film created after strong redox processes as reported elsewhere for other Li-containing coatings.^[7] The remarkable stability of the system over long time, with no sign of imminent coating failure even after 4 weeks immersion, shows much potential for future studies. Moreover, the embedded nanonetwork approach allows for the use of Li-inhibitors in epoxy coatings, thereby increasing their applicability beyond the so far studied polyurethanes.^[7] Nevertheless, the observed strong gas evolution for over 24 h at the damage site is a factor of concern for future research and applications of Lithium inhibitors since unwanted gas evolution under the coating would certainly lead to uncontrolled delaminations and loss of the coating in time. For this reason, and the low inhibiting behavior of the noncrosslinked Ce-containing fiber mat, we opted to further explore the effect of crosslinking on the inhibiting behavior of the nanonetworks just for the case of the cerium-containing fiber mats as shown in Section 2.3.2.

2.3.2. Effect on Corrosion Protection of Nanonetwork Crosslinking

The results for the coating containing a partially crosslinked mat (10CeCL) can be seen in Figure 4d 5, and 6. From the Bode plot in Figure 4 it can be seen that partial crosslinking leads to a very clear improvement compared to the noncrosslinked sample 10Ce. The crosslinked sample shows higher impedance and phase angles in the low-frequency range which remain stable for a long immersion period of up to around 670 h, which is four times longer protection than the noncrosslinked

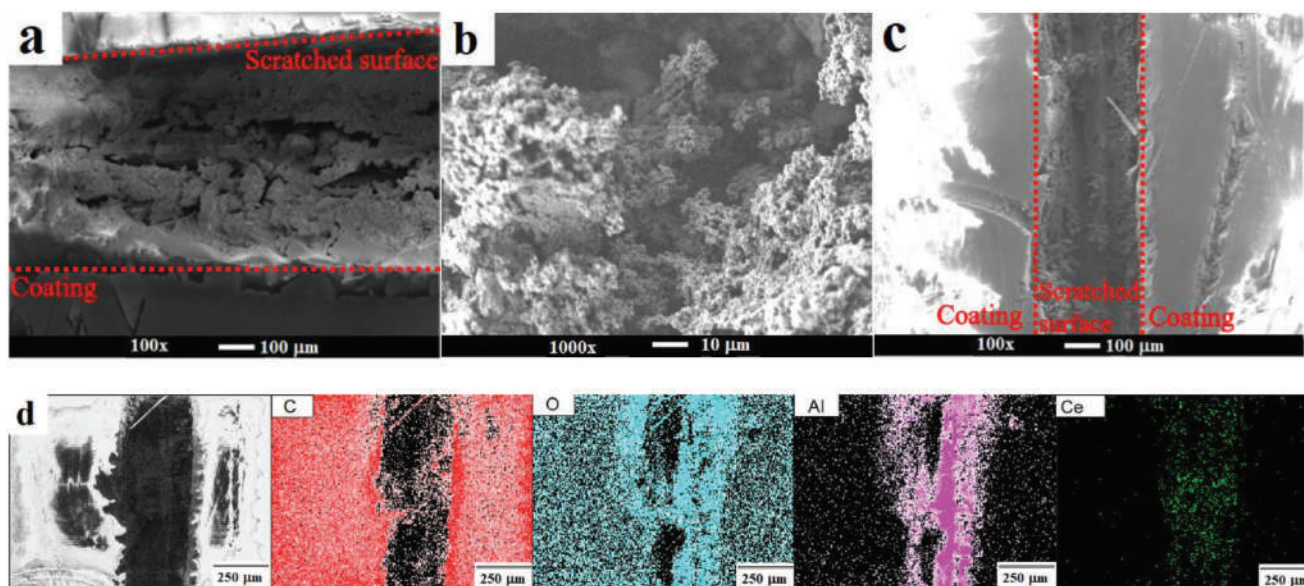


Figure 7. SEM microscopy images of the scribes of a,b) the unloaded PVA and c) the 10CeCL coatings after electrochemical testing. Panel (d) shows the EDS maps of the coating loaded with Ce (10CeCL) after 4 weeks immersion highlighting the presence of cerium in the scratch.

Ce-containing system, and about 11 times longer than results reported with epoxy coatings directly loaded with Ce-salt inhibitors for comparable coatings and damages.^[13] It is worth noting that such numerical differences should be taken as reference and not as definite values as this would require higher sampling for statistical reasons. The comparison becomes more clear when attending to the time evolution plots shown in Figure 5. In this figure it can be seen how the total impedance of the 10CeCL sample is recovered after each sudden drop, this being more evident for the case of the OCP. Drops can here be related to the initiation of corrosion/degradation processes while recovery of the impedance to high values ($10^6 \Omega \text{ cm}^2$) and OCP to values similar to those of AA2024 (-0.5 V) can be related to stabilization/protection of the underlying metal. This is in agreement with the fact that cerium acts as cathodic inhibitor requiring initial redox processes to form insoluble cerium oxides and hydroxides.^[14b] As in the case of the Li-containing coating this behavior is maintained for at least 4 weeks of immersion, the moment at which the experiment was stopped. The image analysis (Figure 6) confirmed the long-term protection with no clear delaminations taking place and the absence of oxide products at the scribe. Nevertheless, at about 4 weeks immersion a delamination became clearly visible on the top right corner of this sample as indicated by a red arrow, thereby highlighting the room for improvement despite the promising results. Nevertheless, the original cause for the presence and evolution of this defect (i.e., formed during scratch or during immersion) needs further investigation.

2.3.3. Postmortem Characterization

At the end of the immersion tests the samples were removed from the electrochemical cells and analyzed (see also Section S6, Supporting Information). In this analysis it was confirmed that

the samples with uncrosslinked PVA fiber led to the delamination of the upper coating at the location of the fiber mat. On the other hand, the 10CeCL coating showed no delaminations after removal of the sample from the testing cell. These observations indicate that (partial) crosslinking helps improving the coating integrity a part from ensuring better and sustained active corrosion protection, although more dedicated research is necessary to improve the crosslinking/inhibitor release balance for long-lasting protection of the nanonetwork concept. Moreover, a dedicated SEM-EDS analysis of the exposed scribes is shown in Figure 7 and Figure S10 (Supporting Information). These figures confirm the high amount of aluminum oxide/hydroxides formed at the scribe in the case of the noninhibited PVA sample (Figure 7a,b and Figure S10, Supporting Information) together with high chlorine concentrations related to the ingress of chloride ions (Figure S10, Supporting Information).^[6a] Figure 7c shows, for the case of the 10CeCL sample, the absence of abundantly formed aluminum oxides in combination with the clear presence of cerium at the scribe (Figure 7d). This confirms the release of inhibitor from the inhibiting network and subsequent formation of protective cerium oxides or hydroxides at the scribe surface thereby reducing the natural aluminum corrosion process.^[18] Raman spectroscopy spectra (Figure S11, Supporting Information) further revealed the presence of cerium rich zones at the same locations of copper-rich phases pointing at the deposition of cerium on copper-rich intermetallic phases and their role as cathodic inhibitor as shown in previous works.^[19,20]

3. Conclusion

In this work, a new concept for long-term corrosion protection at damaged sites in coated panels is presented. The underlying principle is based on the creation of inhibitor interconnections through responsive and low density regions in coatings; what

we here call *inhibiting nanonetworks*. For the proof-of-concept, we used PVA electrospun fiber mats loaded with different corrosion inhibitors and embedded in epoxy coatings on AA2024-T3. The real-time release UV-vis experiments confirmed the possibility to modify the release kinetics and maximum released inhibitor when controlling solubility/swelling and inhibitor loading of the interconnected network. A homemade hyphenated optical and electrochemical setup was used to monitor protection at damaged sites and to confirm long-term corrosion protection up to 4 weeks immersion with two different inhibitors (CeCl_3 and Li_2CO_3). The local analysis of the scribes by means of EDS and Raman spectroscopy confirmed the release of cerium inhibitor and its surface reaction at Cu-rich zones as responsible for the long-term protection at the scribe. On the other hand, the lithium inhibitor led to the formation of a thick protective film, as previously reported in literature, although the observed local gas evolution for over 24 h should be regarded as a factor to be considered in future works and applications. Given the nature of the inhibitors here used it is highly likely that other inhibitors and combinations thereof will lead to even longer corrosion protection. Despite the remaining challenges related to overall coating stability and application, the concept here introduced based on the creation of interconnected high-diffusion paths produced by electrospinning or other manufacturing concepts, opens a new direction for the development of sophisticated, tailored, and highly efficient coatings for the long-term protection of relatively large damages. Even if the concept is here proved by water-triggered inhibitor leaching the principle can be converted to controlled inhibitor release by other trigger mechanisms.

4. Experimental Section

Materials: PVA ($M_w = 88\,000\text{ g mol}^{-1}$, 88% hydrolyzed) was purchased from Acros Organics. GA (50 wt% in H_2O) was ordered from TCI Chemicals. Cerium chloride heptahydrate ($\text{CeCl}_3 \cdot 7\text{H}_2\text{O}$, >99.9%, mentioned in main text as CeCl_3 or simply Ce), lithium carbonate (Li_2CO_3 , >99%), sodium hydroxide (NaOH, > 98%) concentrated hydrochloric acid (HCl, 37%), acetone (ACE, analytical grade), and ethanol (EtOH, analytical grade) were purchased from Sigma-Aldrich. Epikote 828 and Ancamine 2500 were kindly provided by Akzo Nobel. Xylene (99%) was purchased from J.T. Baker. Sodium chloride (NaCl, >98%) was purchased from VWR Chemicals. All aqueous solutions were made with Milipore Elix 3 UV filtered water. Unclad AA2024-T3 alloy sheets with a thickness of 1.5 mm were used as metallic substrate.

Electrospinning of the Inhibiting Nanonetworks: The inhibiting nanonetworks were manufactured using a home-made electrospinning setup. This consisted of a New Era NE-1000 syringe pump, a Spellman Bertan 205B-20R DC power generator with a maximum output voltage of 20 kV, and a grounded aluminum collector plate covered with a supermarket brand bakery release paper for easy removal of fiber networks. 5 mL syringes were loaded with the electrospinning solution with 20G needle with flat tip. The needle was connected to the power supply and the collector plate was grounded. The setup was placed inside a polycarbonate box for safety and humidity and temperature control. A small fan (12 cm diameter) in combination with moisture absorbant was used to keep the relative humidity level (rH) constant at 35–40%, while the temperature was $21 \pm 2\text{ }^\circ\text{C}$ during the electrospinning process.

The electrospinning solutions were prepared by dissolving 8 wt% PVA powder in deionized (DI) water under rapid stirring for up to 24 h. The corrosion inhibitors were added after full dissolution of PVA, in weight

ratios with respect to PVA, to obtain a uniform dispersion of inhibitor through the solution. Neat PVA networks were spun with a potential of 12 kV and a feed rate of 0.4 mL h^{-1} at a distance of 13 cm. CeCl_3 loaded fiber networks (5 or 10 wt% w.r.t. polymer) were spun at the same distance and potential with a feed rate of 0.25 mL h^{-1} . Li_2CO_3 systems were spun with a feed rate of 0.15 mL h^{-1} at a distance of 20 cm with a potential of 20 kV. Fiber mats of around $\approx 10\text{ }\mu\text{m}$ thickness were collected on wax paper for easy removal to be further employed in the release and corrosion protection studies. Both inhibitors fully dissolved in the PVA/ H_2O solution at the studied concentrations.

Partially crosslinking of the mats was performed following the approach of Wang et al. in solution.^[10] For this, crosslinking solutions with different concentrations of GA in acetone were prepared (namely, 10×10^{-3} and $30 \times 10^{-3}\text{ M GA}$). Electrospun fiber networks were placed in these solutions, before adding 37% HCl to obtain a concentration of 0.01 M HCl in the final solution as catalyst for the crosslinking reaction. The fiber networks were kept in solution for 24 h and subsequently dried under N_2 flow and stored in a desiccator until coating procedure. Some samples were placed in H_2O for several days to observe the dissolution behavior.

Substrate Preparation for Coated Panels: Aluminum AA2024-T3 sheets ($30 \times 30 \times 1.5\text{ mm}$) were grinded with subsequently grit 180P and 320P SiC grinding paper to remove the natural oxide layer. To increase the coating adhesion a ScotchBrite 3M “Clean N Finish grade AVFN” was used followed by degreasing the surface with acetone and immersion in 2.0 M NaOH solution for 10 s.^[21] The samples were then immediately rinsed with DI water, dried under N_2 flow, and stored at ambient conditions for 30 min before coating procedure.

Coating with Inhibiting Nanonetworks: Coatings were prepared using different hand-placed electrospun fiber mats. The fiber networks were placed on a $6\text{ }\mu\text{m}$ thick base layer in order to prevent full delamination of the top coat from the metallic substrate. Table 1 shows the characteristics of the coatings discussed in this paper. The epoxy/amine coatings were prepared as discussed elsewhere^[13] by adding epoxy and amine precursors (1:0.58 by weight) and 20 wt% xylene to reduce the coating viscosity and mixed for 5 min in a high-speed shear mixer at 2500 rpm prior to application by spin coating (both the thin base coat as the thick full coating). The $6\text{ }\mu\text{m}$ base layer was applied by spin coating (7000 rpm, 30 s) before hand-placing the fiber network. All samples were then further coated by spin coating step (30 s, 1500 rpm). In order to create uniform smooth films, this last coating step was repeated three times. Subsequently, the coatings were cured at $60\text{ }^\circ\text{C}$ for 24 h. No significant effects of fiber crosslinking on the coating procedure were observed.

Damage Formation of Coated Panels: The different coated panels were intentionally and reproducibly damaged by a CSM Scratch tester (Rockwell indenter, $100\text{ }\mu\text{m}$). 5 mm long, $120 \pm 10\text{ }\mu\text{m}$ wide scratches at the metal substrate were made by multiple passes at increasing forces ($5\text{--}30\text{ N}$, 10 mm s^{-1}) until the substrate was reached.

Characterization Methods: The quality of the fibers in terms of thickness uniformity and bead formation was assessed by spinning them onto glass microscope slides and evaluating them under a Keyence VHX-2000E microscope. Detailed analysis of the fiber mats at high magnification was performed with the help of a field emission scanning electron microscope (FESEM, JEOL-JSM-840, 5 kV working voltage), sticking them on carbon tape placed on a copper/zinc sample-holder, followed by sputtering a 15 nm gold layer to avoid surface charging. Elemental analysis of the fibers was done with help of the EDS system present in the FESEM operating at 15 kV. The elements gold (Au), zinc (Zn), and copper (Cu) in the fiber mats EDS analysis are due to the sample holder and the sputter process. FTIR (Perkin-Elmer Spectrum 100) was used to follow the crosslinking reaction of the fibers in the wavelength range of $4000\text{--}600\text{ cm}^{-1}$.

The release studies of the cerium-based corrosion inhibitor were performed by UV-vis spectroscopy (Perkin Elmer Lambda 35). A quartz cuvette (10 mm path length) was filled with DI water (3 mL) and a fiber mat ($\approx 12\text{ mg}$) was placed in the solution. A small magnetic stirring device with calibrated rotational speed (1000 rpm) was used on the

bottom of the cuvette to ensure fast diffusion of the released inhibitor through the solution in order to measure a uniform distribution. The spectra were taken in the range of interest for cerium signals between 200–325 nm and recorded every 2 min for 2 h.

Coating thickness was measured by an Eddy Current thickness probe. The corrosion protective behavior of the various damaged coatings immersed in 0.05 M NaCl solution over time was analyzed by a specially designed hyphenated optical and electrochemical setup. The electrochemical setup allowed for EIS measurements of an exposed area of 12 mm² and consisted of a three-electrode electrochemical cell with a carbon rod counter electrode and Ag/AgCl double junction reference electrode. A potentiostat (Autolab PGSTAT 302N) allowed the programming and control of the EIS measurements in the frequency range of 10⁻² to 10⁵ Hz at 10 mV RMS amplitude as well as the monitoring of the OCP. OCP and EIS spectra were recorded every hour for a period up to 30 d depending on the goodness of the sample. A microscope camera, coupled to the electrochemical cell, allowed to visually follow the corrosion processes and to take time-lapsed images coinciding with each EIS measurement to better interpret the EIS signals as reported elsewhere.^[13]

After immersion, all samples were examined with SEM and EDS. Several samples were analyzed by Raman spectroscopy (Renishaw InVia Raman, 532 nm, 32 mW laser). Several areas were mapped based on three sequential measurements (50× magnification, 1 s, 100% laser power). The inspected wavenumber range was 300–1000 cm⁻¹.

Supporting Information

Supporting Information is available from the Wiley Online Library or from the author.

Acknowledgements

The authors would like to thank Prof. S. van der Zwaag for his constant support and fruitful discussions. Special thanks also to Dr. I. L. Kyratzis, Dr. Y. B. Truong, and Dr. J. Mardel at CSIRO Clayton, VIC, Australia for introducing the authors to the field of electrospinning, as well as Dr. A. E. Hughes for discussions inspiring this project.

Conflict of Interest

The authors declare no conflict of interest.

Keywords

aluminum alloys, cerium, corrosion protection, electrospinning, lithium

Received: January 30, 2018

Revised: February 23, 2018

Published online:

- [1] a) T. H. Tran, A. Vimalanandan, G. Genchev, J. Fickert, K. Landfester, D. Crespy, M. Rohwerder, *Adv. Mater.* **2016**, *27*, 3825; b) D. Borisova, D. Akçakayran, M. Schenderlein, H. Möhwald, D. G. Shchukin, *Adv. Funct. Mater.* **2013**, *23*, 3799; c) E. L. Ferrer, A. P. Rollon, H. D. Mendoza, U. Lafont, S. J. Garcia, *Microporous Mesoporous Mater.* **2014**, *188*, 8; d) D. Fix, D. V. Andreeva, Y. M. Lvov, D. G. Shchukin, H. Möhwald, *Adv. Funct. Mater.* **2009**, *19*, 1720.
- [2] a) E. Javierre, S. J. Garcia, J. M. C. Mol, F. J. Vermolen, C. Vuik, S. van der Zwaag, *Prog. Org. Coat.* **2012**, *75*, 20; b) D. Crespy, K. Landfester, J. Fickert, M. Rohwerder, *Adv. Polym. Sci.* **2016**, *273*, 247.

- [3] A. E. Hughes, A. Trinchi, F. F. Chen, Y. S. Yang, I. S. Cole, S. Sellaiyan, J. Carr, P. D. Lee, G. E. Thompson, T. Q. Xiao, *Prog. Org. Coat.* **2014**, *77*, 1946.
- [4] T. J. Sill, H. A. von Recum, *Biomaterials* **2008**, *29*, 1989.
- [5] a) A. Balogh, R. Cselkó, B. Démuth, G. Verreck, J. Mensch, G. Marosi, Z. K. Nagy, *Int. J. Pharm.* **2015**, *495*, 75; b) J. S. M. Zanjani, B. S. Okan, I. Letofsky-Papst, Y. Menciloglu, M. Yildiz, *RSC Adv.* **2015**, *5*, 73133; c) S. Ramakrishna, K. Fujihara, W. E. Teo, T. C. Lim, Z. Ma, *An Introduction to Electrospinning and Nanofibers*, World Scientific Publishing Co. Pte. Ltd., London, UK **2005**, Ch.7.
- [6] a) A. E. Hughes, T. A. Markley, S. J. Garcia, J. M. C. Mol, *Corros. Eng., Sci. Technol.* **2014**, *49*, 674; b) M. Bethencourt, F. J. Botana, J. J. Calvino, M. Marcos, M. A. Rodríguez-Chacón, *Corros. Sci.* **1998**, *40*, 1803; c) D. Ho, N. Brack, J. Scully, T. Markley, M. Forsyth, B. Hinton, *J. Electrochem. Soc.* **2006**, *153*, B392; d) M. van Soestbergen, V. Baukh, S. J. F. Erich, H. P. Huinink, O. C. G. Adan, *Prog. Org. Coat.* **2014**, *77*, 1562; e) T. H. Muster, D. Lau, H. Wrubel, N. Sherman, A. E. Hughes, T. G. Harvey, T. Markley, D. L. J. Alexander, P. A. Corrigan, P. A. White, S. G. Hardin, M. A. Glenn, J. Mardel, S. J. Garcia, J. M. C. Mol, *Surf. Interface Anal.* **2010**, *42*, 170; f) J. Carneiro, J. Tedim, S. C. M. Fernandes, C. S. R. Freire, A. J. D. Silvestre, A. Gandini, M. G. S. Ferreira, M. L. Zheludkevich, *Prog. Org. Coat.* **2012**, *75*, 8.
- [7] P. Visser, Y. Liu, X. Zhou, T. Hashimoto, G. E. Thompson, S. B. Lyon, L. G. J. van der Ven, A. J. M. C. Mol, H. A. Terry, *Faraday Discuss.* **2015**, *180*, 511.
- [8] C. Zhang, X. Yuan, L. Wu, Y. Han, J. Sheng, *Eur. Polym. J.* **2005**, *41*, 423.
- [9] M. van Soestbergen, S. J. F. Erich, H. P. Huinink, O. C. G. Adan, *Corros. Eng., Sci. Technol.* **2013**, *48*, 234.
- [10] X. Wang, X. Chen, K. Yoon, D. Fang, B. S. Hsiao, B. Chu, *Environ. Sci. Technol.* **2005**, *39*, 7684.
- [11] a) H. S. Mansur, C. M. Sadahira, A. N. Souza, A. A. P. Mansur, *Mater. Sci. Eng. C* **2008**, *28*, 539; b) C. K. Yeom, K. H. Lee, *J. Membr. Sci.* **1996**, *109*, 257.
- [12] a) R. W. Kormeyer, N. A. Peppas, *J. Membr. Sci.* **1981**, *9*, 211; b) R. W. Kormeyer, R. Gurny, E. Doelker, P. Buri, N. A. Peppas, *Int. J. Pharm.* **1983**, *15*, 25; c) P. L. Ritger, N. A. Peppas, *J. Controlled Release* **1987**, *5*, 37.
- [13] P. J. Denissen, S. J. Garcia, *Corros. Sci.* **2017**, *128*, 164.
- [14] a) T. H. Muster, H. Sullivan, D. Lau, D. L. J. Alexander, N. Sherman, S. J. Garcia, T. G. Harvey, T. A. Markley, A. E. Hughes, P. A. Corrigan, A. M. Glenn, P. A. White, S. G. Hardin, J. Mardel, J. M. C. Mol, *Electrochim. Acta* **2012**, *67*, 95; b) S. J. Garcia, T. A. Markley, J. M. C. Mol, A. E. Hughes, *Corros. Sci.* **2013**, *69*, 346.
- [15] a) E. Darmiani, I. Danaee, M. A. Golozar, M. R. Toroghinejad, *J. Alloys Compd.* **2013**, *552*, 31; b) M. Abdulstaar, M. Mhaede, L. Wagner, M. Wollmann, *Mater. Des.* **2014**, *57*, 325.
- [16] a) T. A. Markley, M. Forsyth, A. E. Hughes, *Electrochim. Acta* **2007**, *52*, 4024; b) P. Campestrini, E. P. M. van Westing, H. W. van Rooijen, J. H. W. de Wit, *Corros. Sci.* **2000**, *42*, 1853.
- [17] a) D. Snihirova, S. V. Lamaka, M. F. Montemor, *Electrochim. Acta* **2012**, *83*, 439; b) I. A. Kartsonakis, E. Athanasopoulou, D. Snihirova, B. Martins, M. A. Koklioti, M. F. Montemor, G. Kordas, C. A. Charitidis, *Corros. Sci.* **2014**, *85*, 147.
- [18] a) P. Campestrini, H. Terry, A. Hovestad, J. H. W. de Wit, *Surf. Coat. Technol.* **2004**, *176*, 365; b) R. Catubig, A. E. Hughes, I. S. Cole, B. R. W. Hinton, M. Forsyth, *Corros. Sci.* **2014**, *81*, 45.
- [19] M. Fabián, B. Antić, V. Girman, M. Vučinić-Vasić, A. Kremenović, S. Suzuki, H. Hahn, V. Šepelák, *J. Solid State Chem.* **2015**, *230*, 42.
- [20] B. L. Hurley, S. Qiu, R. G. Buchheit, *J. Electrochem. Soc.* **2011**, *158*, C125.
- [21] F. M. de Wit, *Ph.D. Thesis*, Delft University of Technology **2012**.